Available online at www.sciencedirect.com

ScienceDirect

Acta Materialia 56 (2008) 4635–4646

Acta MATERIALIA

www.elsevier.com/locate/actamat

Shear striations and deformation kinetics in highly deformed Zr-based bulk metallic glasses

Florian H. Dalla Torre *, Alban Dubach, Justus Schällibaum, Jörg F. Löffler

Laboratory of Metal Physics and Technology, Department of Materials, ETH Zurich, Wolfgang-Pauli-Str. 10, 8093 Zurich, Switzerland

Received 10 April 2008; received in revised form 12 May 2008; accepted 13 May 2008

Abstract

Detailed microscopic observations of the shear surfaces of a deformed, but unfractured, bulk metallic glass sample reveal a wealth of information on the deformation characteristics, kinetics and influence of temperature during serrated flow. The shear surfaces exhibit shear striations, which are similar to those resulting from viscous-like flow in rock-forming minerals. On the shear surface only a few areas show typical vein patterns, the thicknesses of which are less than those known from fracture surfaces. Combined with estimates for adiabatic heating, this indicates that sufficiently high temperatures are already present during shear banding before fracture, though instigated by non-purely adiabatic effects. A kinetic model based on an energy variable which reflects the structural relaxation ability is proposed that accounts for the occurrence of serrated flow combined with negative strain rate sensitivity, and the transition to non-serrated flow, i.e. positive strain rate sensitivity, below a critical temperature and strain rate.

Keywords: Bulk metallic glasses; Adiabatic heating; Deformation kinetics; Structural relaxation; Strain rate sensitivity

---

1. Introduction

Despite the lack of significant plasticity in bulk metallic glasses (BMGs), deformation is highly localized in a few shear bands, where microscopically large shear strains $\gg 1$ take place. Similar to the discrete displacement bursts at shallow depth or low loads observed in single-crystalline metals, shear strain increments of several tens of nanometers are also measured by nanoindentation or microcompression tests in BMGs [1,2]. In single-crystals these "pop-ins" are associated with dislocation nucleation and propagation [3–6], while in BMGs they are associated with the nucleation and percolation of shear transformation zones (STZ) (clusters of several tens of atoms), which lead to macroscopic shear steps [7]. Despite the fundamental structural difference between a single crystal and an amorphous structure, they show some similarities in their mechanical properties: in micropillar compression experiments both materials exhibit similar inhomogeneous flow behaviour with shearing along the angle of the maximum resolved shear stress, which, in contrast to polycrystalline materials, shows a unidirectional orientation of the shear plane in both materials. While the shear surface of a single slip glide plane in crystalline materials is expected to be atomically smooth, a rougher surface can be envisioned in amorphous metals due to their structural disorder. Recent work in micropillar experiments on single-crystalline samples indicates, as expected, smooth glide/shear surfaces [8]. Apart from the interatomic binding potential, it is this configurational atomic arrangement that defines the resistance to shearing (decoupling and recoupling of atomic bonds). Hence a smoother atomic surface exhibits a lower shear resistance/stress than a rougher one. That is why the shear stress for single dislocation events in a single-crystalline sample of conventional size is difficult to discern with a standard mechanical testing setup. Only at sufficiently small sample size and high force resolution (nano-Newton range) are discrete displacement bursts detectable in single-crystals [3–5,9,10]. In BMGs, on the

---

* Corresponding author.
E-mail address: florian.dallatorre@mat.ethz.ch (F.H. Dalla Torre).

1359-6454/$34.00 © 2008 Acta Materialia Inc. Published by Elsevier Ltd. All rights reserved.
doi:10.1016/j.actamat.2008.05.021

other hand, the shear resistance is up to two orders of magnitude higher than in single crystals, and thus a shear event can also be discerned in a macroscopic specimen. One focus of this work is to characterize such shear events in detail.

So far only a few literature reports have paid attention to the surface morphology of shear planes in bulk amorphous metals [11,12]. This is mainly related to the generally small amount of plastic strain occurring before failure, which would otherwise result in large enough shear offsets and thus allow for a more detailed microscopic examination. The observation of the surface morphology of shear planes is important information for the description of possible deformation mechanisms in metallic glasses. Fracture surfaces of metallic glasses, on the other hand, are well known and described by their typical river, vein or other flow patterns [13,14]. These flow features suggest that temperatures well above the glass transition temperature (T_g) are reached at the moment of fracture. Since their first observations, several thermographic experiments have supported the idea of such high-temperature bursts at fracture [15–18]. Some ambiguity with respect to adiabatic heating and the amount of temperature rise associated with shearing before fracture, however, remains, stimulating recent debate as to whether the temperature might be sufficiently high to instigate a localized drop in viscosity and thus promote easy glide along this softened shear zone [17,19–22].

In addition, a comprehensive picture of the deformation kinetics during inhomogeneous deformation in metallic glasses is still not available [23]. Apart from the temperature increase during localized shearing, the shear dilatation models (the STZ model [7] and the free volume or diffusive-jump-like model [24,25]) have found wide acceptance in explaining the drop in viscosity. As also recently reviewed by Schuh et al. [23], these two models, based on a drop in viscosity, contrast with the dislocation approach first adapted to metallic glasses by Gilman and later supported by others ([26–29] and references therein). In contrast to the model of Argon, where the nucleation of STZs (i.e. local clusters of atoms designated as the carriers of motion) reflects the critical step for the activation of shear, in Gilman's model, dislocation-like structures are responsible for the shear deformation. These create the necessary stress field and thus generate the resistance to shear propagation. According to Gilman, the description of the energy needed to cause dilatation and consequently allow for motion of the dislocation over the energy barrier is derived by treating the dilatation as point defects [26]. Therefore, with respect to the dilatational force needed to activate shear, common agreement is found between the various models. In addition, despite the difference in describing the structure and motion of the flow defect, similar thermally activated rate equations have been derived. On the other hand, however, none of the constitutive equations for inhomogeneous plastic flow ascribed by these models addresses sufficiently well the serrated flow as a kinetic phenomenon, this being partially due to the lack of experimental evidence. In this respect we were recently able to show that serrated flow in metallic glasses is strongly correlated with a negative strain rate sensitivity (SRS, $m = \partial \ln \sigma / \partial \ln \dot{\varepsilon}|_{\varepsilon}$) and that the stress–strain curve becomes smooth and the SRS positive below a critical strain rate and temperature [30–32], analogous to the Portevin–LeChâtelier effect known for crystalline solids [33,34].

This paper focuses on the shear morphology of unfractured samples and, based on the experimental observations, discusses the possible influence of local temperature increases during shearing and before fracture. A constitutive equation accounting for the presence and absence of serrated flow as a function of temperature and SRS is presented in light of the microscopic findings. An estimate of the adiabatic heating and the spatial and temporal resolution during compression testing of macroscopic samples is also presented.

2. Materials and methods

$Zr_{57.9}Cu_{22}Fe_8Al_{12}Pd_{0.1}$ and $Cu_{50}Zr_{50}$ prealloys were prepared by arc melting the pure elements (purity >99.995%) in a Zr-gettered argon atmosphere from which cylindrical rods were suction cast into a copper mold having length of ~30 mm and diameters of 3 and 2 mm, respectively. A second batch of compression samples was produced from the same $Zr_{57.9}Cu_{22}Fe_8Al_{12}Pd_{0.1}$ prealloy using an electromagnetic levitation drop-casting technique. Compared to the alloy $Zr_{58}Cu_{22}Fe_8Al_{12}$ [35] the effect of Pd on the glass-forming ability and the amorphous state is not noticeable for the sample sizes studied here. Compression test specimens with a length- to -diameter ratio of 1.7 were cut from these rods and subsequently polished. The amorphous structure of the specimens was confirmed by means of X-ray diffraction (XRD) using a PANalytical X'pert diffractometer with Cu Kα radiation, and by differential scanning calorimetry (DSC) using a Setaram Labsys DSC. The deformed specimens were examined by scanning electron microscopy (SEM) using a LEO 1530 microscope equipped with a field emission gun. Constant cross-head displacement tests and strain rate jump tests in compression were performed on a four-column Schenck–Trebel machine equipped with a 100 kN load cell. Tests were performed at various cross-head velocities ranging from 1.0 to 0.1 mm min^{-1}, resulting in initial strain rates of 3×10^{-3} to 3×10^{-4} s^{-1}. The strain was measured from the cross-head displacement and a strain gauge positioned on the pistons above and below the specimen. Acquisition rates of 20–1200 Hz were used to provide information on the shear band velocity. Oxygen contents ranging from 200 to 300 ppm were measured using a LECO TC-436 oxygen analyzer with 80–100 mg samples. Transmission electron microscopy (TEM) experiments were performed with Philips CM20 and CM300 microscopes operating at 200 and 300 kV, respectively. TEM samples of the undeformed material were prepared by mechanical dimpling for ~30 min followed by ion milling with a 3 keV argon beam. One TEM sample cut from the deformed material of the shear plane surface shown in Fig. 1 was prepared using a focused-ion beam (FIB). After electron-beam and ion-beam deposition of a surface protective layer of a total thickness of 2 μm Pt, the TEM sample was thinned down to ∼110 nm with a final beam current of 50 μA of Ga^+ -ions.

3. Results

3.1. SEM observations of a shear plane surface in $Zr_{57.9}Cu_{22}Fe_8Al_{12}Pd_{0.1}$

Fig. 1 shows a stress–strain curve (a) and the corresponding deformed specimen (b). It has been compressed without fracture to more than 20%. The change in the slope of the stress–strain curve is associated with the geometrical changes in the cross-sectional area during shearing. Due to the frictional forces between the sample and the compression plates, cohesion of the sample is additionally supported once the top part of the sample makes contact with the lower compression plate (constrained plasticity). At this moment the stress in Fig. 1a increases again and fracture of the sample becomes less critical due to the continuously decreasing aspect ratio (length/diameter). The inset in (a) shows the gradual increase in the stress drop magnitude (serration amplitude, $\Delta\sigma$) as a function of strain. The peak in the magnitude correlates with the maximum stress reached in the stress–strain curve (neglecting the ill-infected part of the stress–strain curve beyond a strain of 0.25). A plastic strain as high as that shown in Fig. 1 is about 10 times larger than that generally reached in BMGs and is for the unconstrained part attributed to the pre-existence of nanosized crystals dispersed in the amorphous matrix which have been nucleated during solidification (Fig. 2). The positive influence of nanosized crystals embedded in an amorphous matrix on the plastic strain has previously been reported by various authors [36,37].

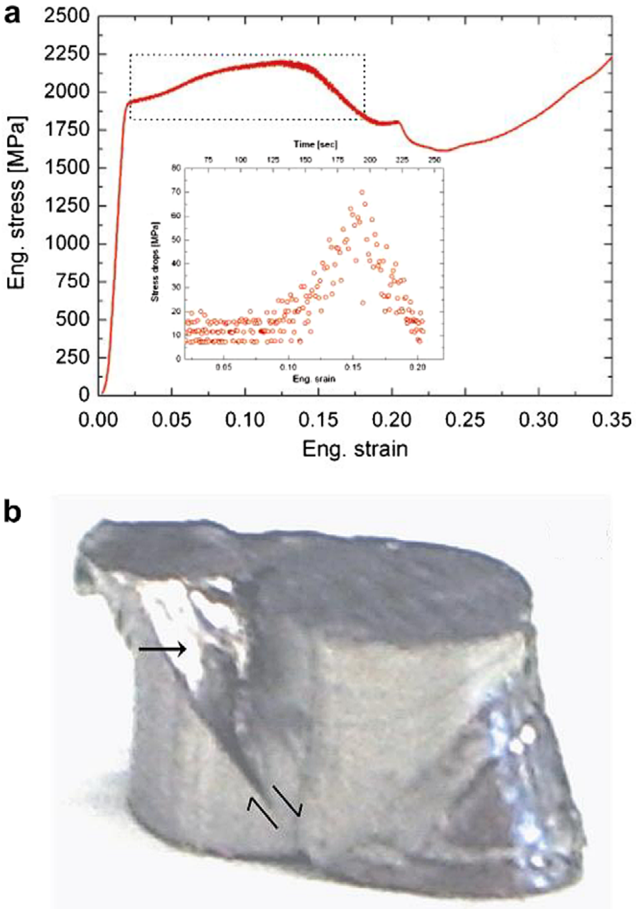

Fig. 1. (a) Stress–strain curve of a $Zr_{57.9}Cu_{22}Fe_8Al_{12}Pd_{0.1}$ sample deformed at room temperature and an initial strain rate of $1 \times 10^{-4}\ s^{-1}$. The inset in (a) shows the increase in the stress drop magnitude with strain recorded within the dotted square. The maximum stress drop correlates well with the ultimate compressive stress reached. (b) Corresponding deformed specimen; the vector arrows indicate the shear direction, while the single arrow indicates the shear surface examined by SEM.

Figs. 3–5 show different areas on the sheared surface. Fig. 3 shows the linear shear striations that cover 90% of the totally sheared and revealed shear surface. These shear striations bear similarities in appearance to those known in ductile shear zones of rock-forming minerals (mylonites), which form as a consequence of shear softening towards a semi-fluid state that allows for quasi-viscous flow [38,39]. The big arrows in the figures indicate the direction of shear on the surface made by the top part of the compression specimen (right-hand side in Fig. 1b). Detailed examination of the major shear band plane indicates that it is laterally separated into many smaller shear surfaces. They are separated by vertical steps facing opposite direc-

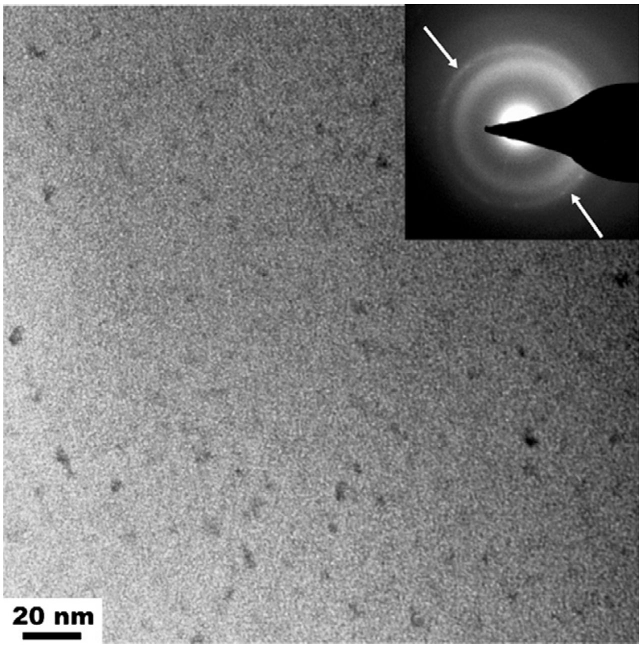

Fig. 2. Bright-field image with selected area diffraction (SAD) pattern indicating the presence of nanosized crystals embedded in the amorphous matrix of the alloy $Zr_{57.9}Cu_{22}Fe_8Al_{12}Pd_{0.1}$. The second ring in the SAD pattern, indicated by the arrows, confirms the crystallinity of the darker nanosized contrasts shown in the bright-field image.

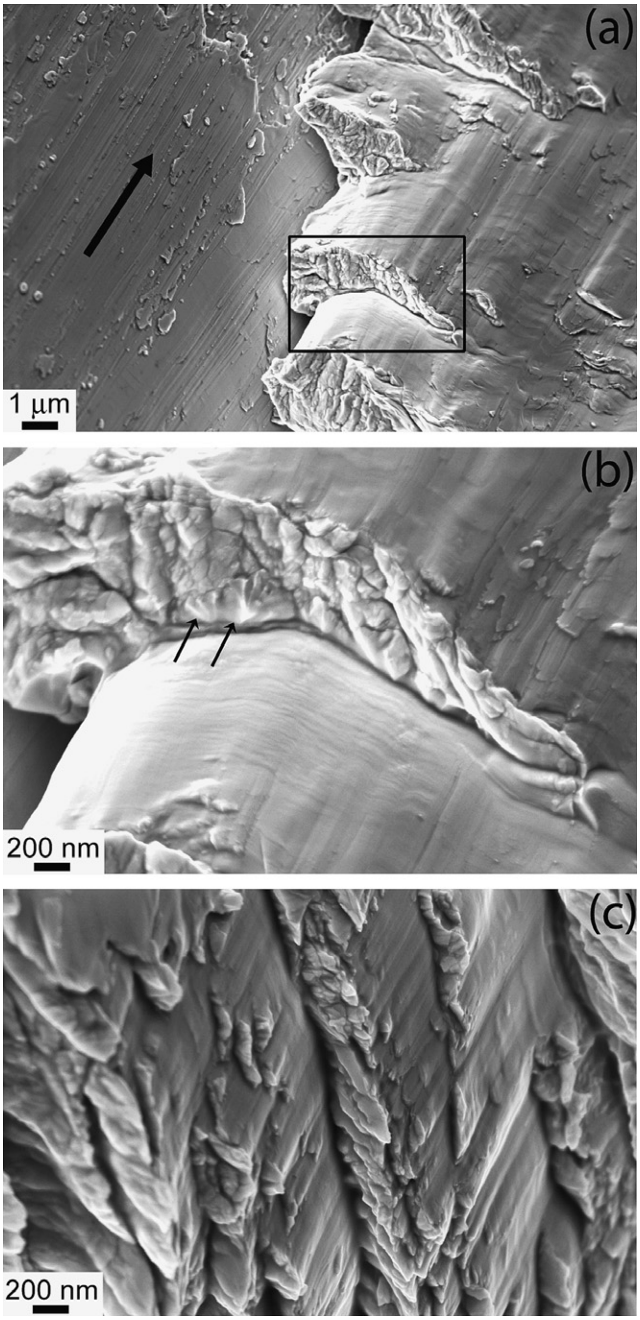

Fig. 3. Shear striations indicating the direction of shear (big arrow) together with shear step surfaces oriented perpendicularly to the shear plane of the $Zr_{57.9}Cu_{22}Fe_8Al_{12}Pd_{0.1}$ sample shown in Fig. 1. The close-up (b) of one of the shear step surfaces (see square in (a)) shows a brittle fracture mechanism with microcracks and a ductile fracture mechanism indicated by the vein pattern (see arrows in (b)). The spacing of single shear planes can be as narrow as tens to few hundreds of nanometers (c).

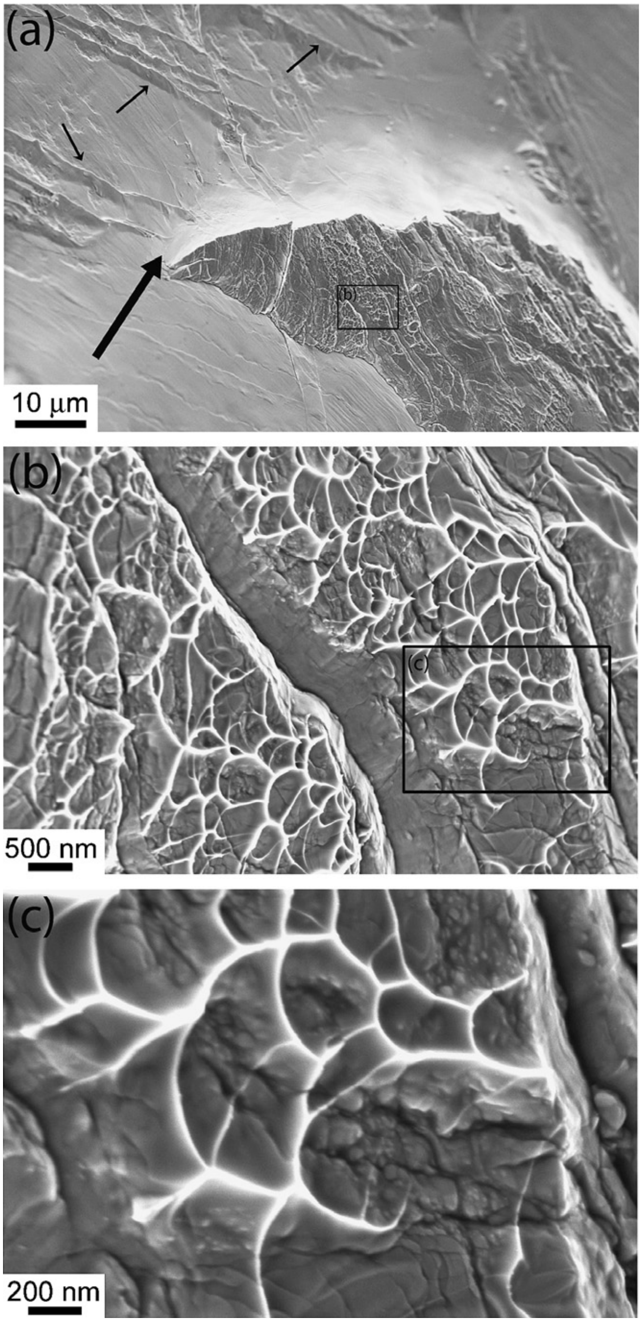

Fig. 4. SEM images recorded on the shear plane surface of the deformed $Zr_{57.9}Cu_{22}Fe_8Al_{12}Pd_{0.1}$ sample shown in Fig. 1. The small arrows in (a) indicate the intersection of the major shear plane with a minor one; the large arrow indicates the direction of shear of the major shear plane. The vein pattern observed on the triangular feature is of shallow depth and reveals a more brittle mode lying underneath (c).

tion of shear, i.e. they form a gentle upward-walking staircase structure. The same orientation of the topological shear steps has recently been observed on a shear surface of a Pd-based BMG which was deformed during micropillar compression experiments [2]. Closer inspection of these shear step surfaces indicates that the majority shows a brittle fracture mechanism where a high density of shear bands or microcracks intersect, being roughly 100 nm or less apart. On the surfaces of the shear steps only a few areas indicate a viscous fracture type, where onsets/nucleations of vein patterns are visible (smaller arrows in Fig. 3b). Interestingly, these vein patterns occur at the foot of the steps, where shearing along the lower plane is assumed to be more pronounced. Some areas indicate a very narrow separation of shear steps (Fig. 3c). This indicates that the

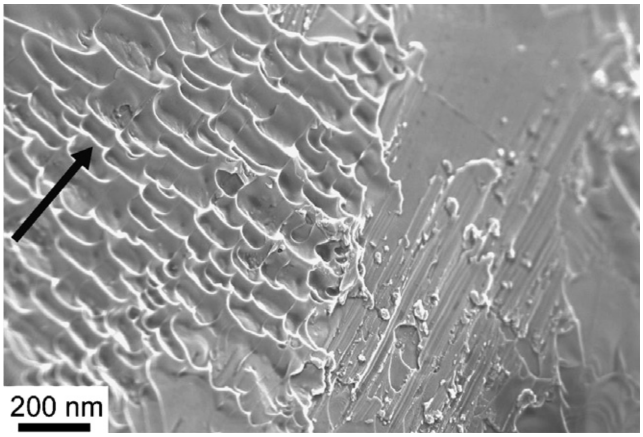

Fig. 5. Area showing viscous flow features in the near neighbourhood of shear striations, which have the same shear plane surface as in Fig. 4.

major shear plane, or more generally speaking a macroscopically visible major shear band of a deformed sample, is not sheared solely on one plane, but is sheared along a whole shear zone consisting of many parallel spaced, smaller shear planes. The spacing of these smaller shear planes can be as close as several tens of nanometers, which is of the same order of magnitude as the nanosized crystals embedded in the amorphous matrix shown in Fig. 2. It is not clear from this observation whether the magnitude of the shear band spacing is dictated by the nanosized crystals, this might explain the increased plasticity in the sample [36,37].

Fig. 4 shows a set of SEM images taken from another shear step on the shear plane, which compared to the shear steps shown in the previous figure does not have a 90° orientation, but is rather at a greater angle to the shear plane surface in front of it. The triangular feature highlighted by a square and shown in greater detail in Fig. 4b and c is to a large extent covered with vein patterns otherwise known only for fracture surfaces. Closer inspection of these vein patterns, however, indicates an important difference compared to fracture surfaces of metallic glasses. Here the vein pattern is very thin and reveals a dense net of shear bands or microcracks underneath, which suggests localized brittle behaviour superimposed by a viscous mechanism. In contrast, fractured surfaces are smooth throughout their entire visible depth of a few micrometers (see e.g. Fig. 2b in Ref. [31]). Moreover, as shown in Fig. 4b, the veins seem to be localized by shear bands, acting either as source of these viscous flow patterns or as a barrier.

Only a few areas on the shear surface were found which exhibit vein patterns and shear striations near each other with the same planar orientation (Fig. 5). This resemblance between the patterns suggests that the thermal histories of both structures are similar. Thus the shear striations can be explained as smeared-out, viscous-like features, which compared to the vein patterns experienced a more intensive compressive shear stress component before exposure of the surface. Note that similar features also result from tribological wear resistance tests performed on BMGs [40].

3.2. TEM investigation of the shear surface in $Zr_{57.9}Cu_{22}Fe_8Al_{12}Pd_{0.1}$

Fig. 6 shows the cross-section of a shear striation in TEM dark-field mode together with a selected area diffraction (SAD) pattern taken from this area. The sample was prepared by FIB and cut from the shear plane surface of the deformed sample shown in Fig. 1. The arrows indicate areas of different contrast, which are taken as an indication of a change in the atomic structure with respect to the bulk. The sharper straight contrast has a thickness of 15 nm, similar to what has been measured by other TEM observations for the thickness of a shear band [41–45]. The less distinct contrast with a sigmoidal shape extends over a width of close to 100 nm. The SAD pattern (inset in Fig. 6) taken from this heavily sheared area (shear striation) indicates no crystalline order. Although shear-induced crystallization has been proposed as a mechanism in other BMGs [37,45] it is not assumed to take place in the samples studied here.

3.3. Deformation curves and sensitivity on temperature and strain rate

Fig. 7 shows a stress–strain/load–displacement curve taken from a $Zr_{57.9}Cu_{22}Fe_8Al_{12}Pd_{0.1}$ sample exhibiting large ductility (~6%). Similar to the stress–strain curve shown in Fig. 1, an increase in the stress drop magnitude occurs with increasing strain. This is associated with the continuous reactivation of the same shear band. The

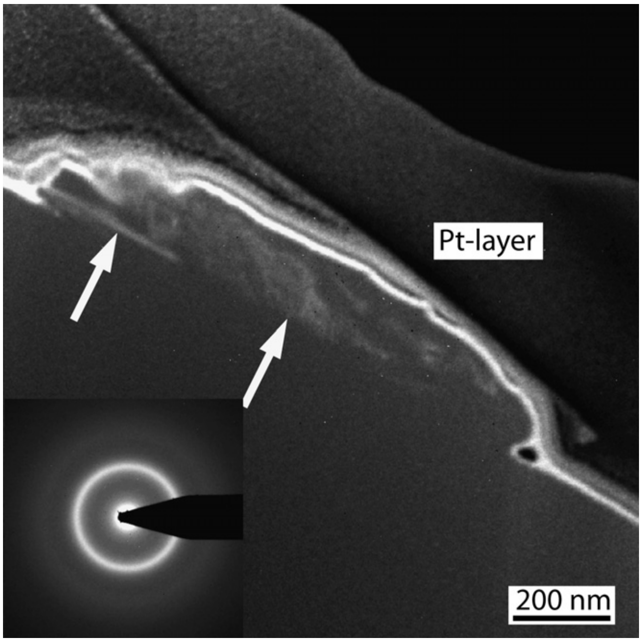

Fig. 6. TEM dark-field image together with SAD pattern taken from the deformed sample shown in Fig. 1. The sample cut by focused-ion beam represents a cross-sectional view of a shear striation. The top part shows the protective Pt layer.

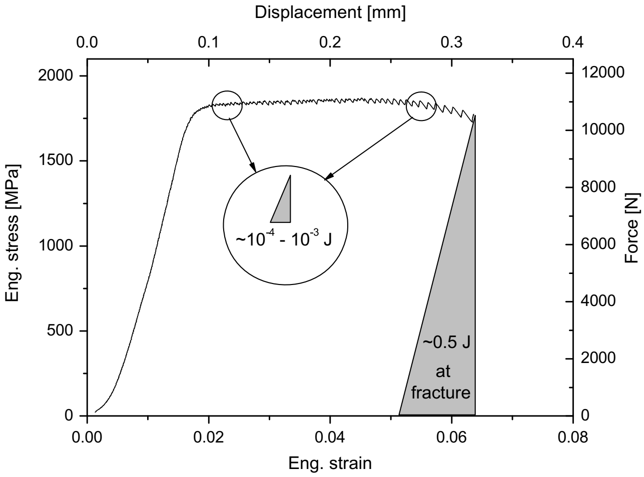

Fig. 7. Stress–strain and force–displacement diagram of inhomogeneous deformation in $Zr_{57.9}Cu_{22}Fe_8Al_{12}Pd_{0.1}$. The triangles represent the work released during one serration cycle and during fracture.

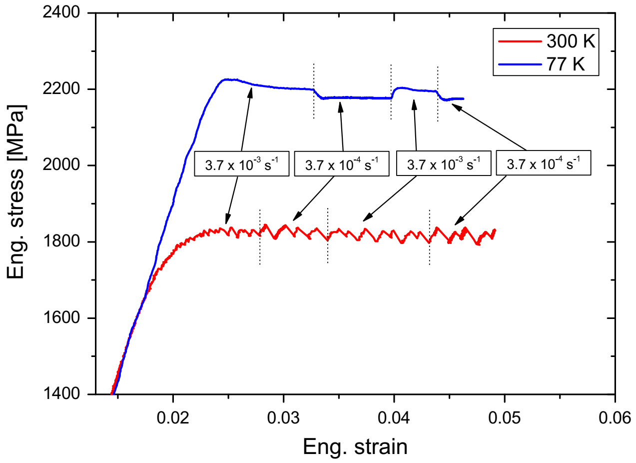

Fig. 8. Stress–strain curves of $Zr_{57.9}Cu_{22}Fe_8Al_{12}Pd_{0.1}$ measured at 77 and 300 K by alternating the strain rate from 3.7×10^{-3} to $3.7 \times 10^{-4}\ s^{-1}$.

energy release (ΔE) by a single stress drop, represented by the triangles in Fig. 7, can be estimated by

$$\Delta E = \int \vec{u} \cdot \vec{F} \cong \vec{u} \cdot \vec{F}/2, \qquad (1)$$

where $\vec{u}$ is the axial displacement and $\vec{F}$ the force applied. The conversion from the displacement measured parallel to the loading direction (Δu) to that of a shear plane oriented ~45° with respect to the compression direction (Δw) is obtained by simple geometric relationships. A steady increase in the energy release with increasing stress drop magnitude (see also inset of Fig. 1) can be estimated and ranges from $\sim 10^{-4}$ to $\sim 10^{-3}$ J. Correcting for machine stiffness and the effect of damping on the load cell values, a factor 2–3 higher may be expected [46]. At the moment of fracture, however, the energy release is about three orders of magnitude larger and reaches values close to 1 J. The fracture surfaces observed here, and also in other BMGs as described in numerous previous publications, show smooth, micrometer-thick river patterns throughout the entire samples which are a result of viscous flow at fracture. This suggests that the heat release during fracture is sufficiently high to melt the entire fracture surface. Thus, based on the difference observed on shear planes and fracture surfaces, we conclude that temperatures during shearing before fracture are significantly lower and thus might cause far less local melting.

For temperatures well below room temperature, we showed recently that serrated flow is no longer present and that the deformation kinetics changes [30,31]. This scheme is also valid for the alloy $Zr_{57.9}Cu_{22}Fe_8Al_{12}Pd_{0.1}$, as shown in Fig. 8. Two stress–strain curves produced from the same sample batch are shown—one measured at 77 K and one at 300 K. The strain rate $\dot{\varepsilon}$ was alternated between 3.7×10^{-3} and $3.7 \times 10^{-4}\ s^{-1}$. As indicated in Fig. 8 and also quantitatively expressed in Table 1 for this alloy and in more detail for the binary BMG $Cu_{50}Zr_{50}$ (see also Ref. [30]), a decrease in the steady-state SRS $\left(m = \left(\frac{\partial \ln \sigma}{\partial \ln \dot{\varepsilon}}\right)_{\varepsilon}\right)$ from values of 0.004 at 77 K to values of approximately −0.002 at 300 K have been measured. This change in the deformation kinetics strongly suggests a fundamental change in the deformation mechanism.

In the following section, estimates of temperature increase in the shear bands are discussed by revisiting the general heat conduction equations (also presented recently in Refs. [11,17,18,20,23]). In this context a critical discussion of the values deduced from stress–strain analyses combined with the information obtained by SEM on shear surfaces is crucial for giving correct answers to questions on the temperature increase during shearing in BMGs. In addition, we will discuss the influence of temperature on the appearance and disappearance of serrated flow and correlate it with a model we recently proposed for the description of the flow kinetics [31] and the recently found analogy

Table 1
Strain rate sensitivity values for the $Zr_{57.9}Cu_{22}Fe_8Al_{12}Pd_{0.1}$ alloy and binary $Cu_{50}Zr_{50}$ measured at various temperatures for a mean strain rate of $2 \times 10^{-3}\ s^{-1}$

Sample	Temperature (K)			
	300	195	153	77
$Zr_{57.9}Cu_{22}Fe_8Al_{12}Pd_{0.1}$	-0.0021 ± 0.0002	n.m.	n.m.	0.0035 ± 0.0005
$Cu_{50}Zr_{50}$	-0.001 ± 0.0002	0.000 ± 0.001	0.001 ± 0.001	0.004 ± 0.001

The error results from the variation of the measured values. The abbreviation n.m. stands for not measured.

to the Portevin–LeChâtelier effect known for crystalline alloys [32].

4. Discussion

4.1. Application of heat conduction equations to BMGs

Significant attention has recently been paid to the influence of adiabatic heating during shear banding [11,17–22,47]. In several works thermographic measurements were applied in situ during compression testing in an attempt to capture the possible temperature increase during shear banding and fracture [17–19,22,47]. Hufnagel et al. [17] pointed out the importance of the heat conduction velocity, which at least under quasi-static deformation conditions is sufficiently high that adiabatic heating does not play a major role. At fracture an increase in temperature has been measured in several BMGs, closely corresponding to the glass transition temperatures (T_g) [18,22,47]. Although these conclusions are supported by heat conduction equations, their temporal and spatial resolution is limited. To circumvent this, Lewandowsky and Greer recently proposed a fusible tin coating as a method to evaluate the spatially and temporally restricted temperature rise during shear banding [21]. Their results demonstrate that although adiabatic heating might not be valid, very high temperatures ($\gg T_g$) can result from localized deformation in shear bands. In accordance with this thinking we demonstrate here, based on our mechanical testing results, that heat conduction has indeed to be considered as the relevant parameter controlling temperature, and discuss whether serrated flow parameters can provide valuable information in this respect.

The general equation used to describe adiabatic heating processes takes the form of an energy density (J m^{-3}) and is written as

$$\rho c_p \Delta T = K \Delta\tau \Delta\gamma, \tag{2}$$

where ρ is the density (here the theoretical density at room temperature is 6.7 g cm^{-3}) and c_p is the specific heat (here estimated to ~380 J kg^{-1} K^{-1} which is in the same range as values used for other Zr-based BMGs [48,49]). On the right-hand side of Eq. (2), K is a constant (~0.9) related to the amount of plastic work that is converted into heat [50]. Eq. (2) shows that the temperature increase ΔT during adiabatic shear banding is directly proportional to the amount of shear strain ($\Delta\gamma$) times the shear stress ($\Delta\tau$) generated. If we assume that the incremental shear strain $\Delta\gamma$ is equal to the time Δt elapsed during the activation of a shear event multiplied by the shear strain rate, $\dot{\gamma}(\Delta t = \Delta\gamma/\dot{\gamma})$, Eq. (2) can be written in the form [17,51]:

$$\Delta T = \frac{K \Delta\tau \dot{\gamma}}{\lambda} x^2, \tag{3}$$

where λ is the thermal conductivity (in W m^{-1} K^{-1}), which is related to the thermal diffusivity, α (in m^2 s^{-1}), by $\lambda = \alpha\rho c_p$. The spatial variable $x = \sqrt{\Delta t \alpha}$ represents the heat-affected zone perpendicular to the direction of shear displacement. More recent theoretical considerations [19,21] for the case of adiabatic shear banding in BMGs were adapted from calculations by Eshelby and Pratt [52] in which the heat generated by a dislocation moving on a slip plane was estimated. Here, the temperature increase can be written in the form of [19,21]:

$$\Delta T = \frac{\Delta\tau \dot{w}_{\mathrm{displ}}}{\lambda} \sqrt{\frac{\alpha \Delta t}{\pi}}, \tag{4}$$

where $\dot{w}_{\mathrm{displ}}$ is the plastic shear displacement rate (a velocity).

From Eqs. (3) and (4) it becomes evident that the crucial parameters dictating the amount of adiabatic heat generated are the shear stress, the time elapsed during shear banding and the width of the heat-affected zone in a shear band. Fulfilling the condition of adiabatic heating, the thickness of the heat-affected zone x can be estimated according to $x = \sqrt{\Delta t \alpha}$, with $\alpha \approx 3.2 \times 10^{-6}$ m^2 s^{-1} at T_g for Zr-based BMGs [53]. If assuming $x \sim$ shear band thickness, which has been estimated to be in the range of a few tens of nanometers [41–45], then time-periods in the range of nanoseconds would have to be envisioned for the activation of a shear band in order to reach temperatures close to T_g (and thus the above-mentioned diffusivities) within a shear band. In agreement with previous results obtained from compression tests recorded at intermediate acquisition rates [11,17,19], the magnitude of Δt measured (see Table 2) is in the millisecond range. This means that to fulfil the adiabatic condition a heat-affected zone x of several tens to hundreds of micrometers would be expected. As already noticed by Ref. [17] this is, however, several orders of magnitude larger than the expected width of a shear band observed by TEM.

Table 2 presents values for parameters deduced from a representative stress–strain curve such as the one shown in Fig. 7. As indicated, the columns are separated into an early, medium, late and fracture stage during compression testing. Here Δt is taken as the time required for a shear band to initiate, propagate and become arrested, i.e. the time needed for a stress drop ($\Delta\sigma$) or failure to occur. In contrast to previous reports, it is assumed that the energy provided to cause a possible temperature rise is not the applied total stress, but the released stress during shearing, i.e. a stress drop. As shown, both the stress drop magnitude and the resulting shear displacement (Δw) or overall strain increment ($\Delta\varepsilon$) increase in the course of deformation, while the time-periods Δt remain roughly constant. Depending on the shear band thickness chosen, a large variation in shear strain rates $\dot{\gamma}$ of 10^4–10^8 s^{-1} can result. This illustrates how crucial knowledge of x is for estimating the shear band temperature. In Table 2 temperature increases ΔT using Eqs. (3) and (4) are presented for various values of Δt and x. Inserting small values for x and Δt results in high values for $\dot{\gamma}$ and ΔT. In addition $\dot{\gamma}$ and ΔT gradually increase with strain to fracture. The calculations show that at fracture temperatures may reach values of several

Table 2
Typical measured and calculated values associated with a shear event at room temperature and an intermediate strain rate of $5 \times 10^{-4}\ \mathrm{s}^{-1}$ for a Zr-based BMG

Serrations at:		Initial	Medium stage	Late stage	Fracture
Measured					
$\Delta\sigma = \Delta\tau$ (MPa)		10 ± 5	20 ± 10	45 ± 15	1900
ΔF (N)		40 ± 15	120 ± 50	230 ± 50	11000
$\Delta\varepsilon$		$4 \times 10^{-4} \pm 1 \times 10^{-4}$	$5 \times 10^{-4} \pm 1 \times 10^{-4}$	$1 \times 10^{-3} \pm 5 \times 10^{-4}$	1×10^{-2}
$\Delta u = \sqrt{2}/2 \cdot \Delta w$ (μm)		1.0 ± 0.5	1.5 ± 0.7	3.0 ± 1.5	12.0 ± 3
$\Delta t_{\mathrm{measured}}$ (ms)		30 ± 20	50 ± 20	70 ± 20	50 ± 20
Calculated					
$\dot{w}_{\mathrm{displ}} = \Delta u/2\Delta t$ (m s^{-1})	Using $\Delta t_{\mathrm{measured}}$	1.7×10^{-5}	1.5×10^{-5}	2.1×10^{-5}	1.2×10^{-4}
$\Delta\gamma = \Delta w/x$	Using $x = 10$ nm	50	75	150	600
$\dot{\gamma} = \Delta\gamma/\Delta t$	Using $x = 10$ nm, $\Delta t_{\mathrm{measured}}$	1667	1500	2143	12000
$\dot{\gamma} = \Delta\gamma/\Delta t$	Using $x = 10$ nm, $\Delta t = 100$ μs	5×10^{5}	7.5×10^{5}	1.5×10^{6}	6×10^{6}
	Using $x = 10$ nm, $\Delta t = 5$ μs	1×10^{7}	2×10^{7}	3×10^{7}	1×10^{8}
ΔT (K) Eq. (3)	Using $x = 10$ nm, $\Delta t_{\mathrm{measured}}$	9.7×10^{-5}	1.8×10^{-4}	6.3×10^{-4}	0.133
	Using $x = 10$ nm, $\Delta t = 100$ μs	2.9×10^{-2}	8.8×10^{-2}	4.4×10^{-1}	67
	Using $x = 10$ nm, $\Delta t = 5$ μs	0.6	1.8	8.8	1331
ΔT (K) Eq. (4)	Using $\Delta t_{\mathrm{measured}}$	1.8	4.3	18	3230
	Using $\Delta t = 100$ μs	31.7	95.0	475.2	72235
ΔW (J/m^3) Eq. (5)		2.5×10^{8}	7.5×10^{8}	3.4×10^{9}	5.7×10^{11}
ΔH (J/m^2)	Using $x = 10$ nm	2.5	7.5	37.5	5700

Here Δt, ΔF and Δu are measured values for the time elapses, the force drop and the displacement associated with a shear event, whereas the stress drop $\Delta\sigma$, shear stress drop $\Delta\tau$, the shear displacement Δw and the strain increment $\Delta\varepsilon$ are deduced from these values. Calculated values are the overall displacement rate $\dot{w}_{\mathrm{displ}}$, the local shear strain $\Delta\gamma = \Delta w/x$ of a shear band with thickness x, and the shear strain rate $\dot{\gamma}$. For simplicity, the dimension x is here taken as the shear band width as well as the thickness of the heat-affected zone. The adiabatic temperature increase ΔT (see Eqs. (3) and (4)) is also given, together with values for the heat content ΔH and energy density ΔW in a shear band.

thousand degrees Celsius, but before fracture temperatures are far too low to explain the observed viscous flow features in Figs. 4 and 5. Rewriting Eq. (1) in the form of stress and strain yields (as in Eq. (2)) an energy density [54]:

$$\Delta W = \int_0^{\Delta t} \sigma(t)\dot{\varepsilon}(t)\mathrm{d}t = \Delta\sigma\Delta\varepsilon, \tag{5}$$

which multiplying by $x = 10$ nm results in a heat content ΔH. The values shown in Table 2 for ΔH and ΔW are, for the energy released at fracture, within the same range as those of Refs. [21,54], while before fracture the values are two orders of magnitude lower.

4.2. Validation of parameters Δt; $\Delta w, \dot{w}_{\mathrm{displ}}, \dot{\gamma}$, and x

4.2.1. Validation of Δt

To evaluate the validity of the adiabatic condition $x = \sqrt{\Delta t \alpha}$ we investigated in detail the stress drop behaviour and Δt with respect to the acquisition rate up to 1200 Hz. As shown in Table 2, Δt is of the order of tens of milliseconds irrespective of the size of the stress drop or the acquisition rate chosen. This indicates that the ratio $\Delta\sigma/\Delta t$ increases with increasing strain from values of ~300 to ~700 MPa s^{-1}, i.e. the speed of the stress drop magnitude increases by at least a factor of two.

Acoustic emission (AE) associated with shear band activity provides further temporal resolution. Due to its fast propagation speed it causes almost no delay time between the occurrence of a shear band event and its recording. Vinogradov et al. [55] performed detailed acoustic emission measurements during compression testing of a Zr-based metallic glass ($\mathrm{Zr}_{52.5}\mathrm{Ti}_5\mathrm{Cu}_{17.9}\mathrm{Ni}_{14.6}\mathrm{Al}_{10}$) and found that acoustic signals occur well before a stress drop can be recorded in the stress–strain diagram. In addition, their results suggest that the shear band propagation during a stress drop is characterized by sequential multiple "stops and goes", giving rise to packets of intense AE pulses, each spaced by 2–3 μs, resulting in a packet width of approximately 50–500 μs. In our view this period can be taken as the minimal time needed for a stress drop to be recorded during mechanical testing. Thus it gives a lower boundary for the time Δt in which a shear band nucleates, propagates and becomes fully arrested. Considering the possible temperature variation triggered by a shear event in a shear band, Δt can also be regarded as the time required for heating and quenching of the sheared volume. Assuming maximum temperatures of the order of T_g this would result in quench rates within a shear band of $>10^5$ °C s^{-1}. On the other hand, our copper mould casting systems reaches maximum quench rates of $\sim 10^3$ °C s^{-1} [56]. Therefore, and in accord with our TEM observations on the deformed sample (Fig. 6), strain-induced nanocrystallization seems to be unlikely.

4.2.2. Validation of $\Delta w, \dot{w}_{\mathrm{displ}}, \dot{\gamma}$

In order to evaluate whether these stress drops microscopically represent single shear events on an existing shear band or rather a sum of instantaneously released, newly nucleated shear bands, the shear surface was closely inspected (see Fig. 9). The slight but distinct slips perpendicular to the shear striations on the shear surface (direction of shear indicated by the arrow) suggest that they arise from temporally separated reactivation of the same shear band by single shear offsets or events. Here we refer to single shear events as the stress drops recordable during compression testing. Measuring the distance between these marks reveals values of 200 nm–2 μm, which are of the same order of magnitude as the shear displacements (Δw) measured from stress–strain curves (Table 2). This observation allows for a more confident estimate of the displacement rate ($\dot{w}_{\mathrm{displ}}$) and shear strain rate ($\dot{\gamma}$) and confirms that spatially and temporally the stress drops can be taken as single shear events occurring along one single shear band. To the knowledge of the authors such a correlation between the details of a stress–strain diagram and microscopic shear slips seen on shear surfaces of metallic glasses has not been observed previously.

4.2.3. Validation of x

As supported by numerous TEM studies of shear bands [41–44], and in agreement with the observation made here, the width of a shear band extends generally only over a few tens of nanometers. SEM observations, in contrast, suggest that the thickness of the liquid-like fracture surfaces is significantly larger: on the order of several hundred nanometers to a few micrometers [13,14,20]. Thickness estimates from our SEM investigations confirm this. Furthermore, Figs. 4 and 5 strongly suggest that liquid-like morphologies can be present on the shear surfaces before fracture with thicknesses of only several tens of nanometers—in agreement with the TEM observations. We, therefore, assume that localized compressive stress release promotes growth of the liquid-like structure. Further, the heat within shear bands (which senses compressive stress) is conducted more efficiently in compressive conditions than on surfaces that shear with a localized tensile stress component. TEM observations commonly exhibit shear bands sandwiched in between non-deformed material and thus must have, due to cohesion of the material, experienced a strong compressive component. This allows for sufficiently high heat conduction and thus for formation of only thin, nanometer-sized shear bands. Values for the propagation time of shear bands (Δt) of a few microseconds, as suggested by AE measurements [55], produce a width for the heat-affected zone within the range of the liquid-like structures observed on the fracture surfaces (i.e. hundreds of nanometers to a few micrometers), so that adiabatic conditions are assumed to be fulfilled at fracture. Before fracture, more ambiguity remains with regard to adiabatic conditions as demonstrated in Table 2, despite the fact that high temperatures of several hundred degrees have been estimated [21]. This strongly suggests that the shear band thickness is not equivalent to the thermal diffusion length x, which would have to be significantly larger to achieve adiabatic conditions. This discrepancy in the dimensions of x and the shear band width was also considered in Ref. [57], where it was concluded that shear localization is attributed to a structural (dilatation) change rather than to adiabatic heating and that heat generation may be a cause of shear localization.

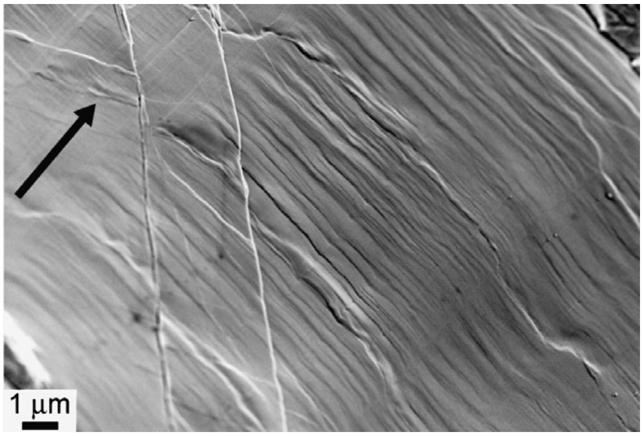

Fig. 9. Signature of discrete shear slip events on the shear surface oriented perpendicular to the shear direction (arrow) in $Zr_{57.9}Cu_{22}Fe_8Al_{12}Pd_{0.1}$. These slip marks are proof of the reactivation of a pre-existing shear band. The distances of the slip marks are of the same dimension as the displacement measured from a stress drop in the deformation curve. Note that stick–slip on shear planes in rocks yield similar surfaces features.

In summary, explaining the local melting seen in the SEM images of Figs. 4 and 5, the following can be deduced from Eqs. (3) and (4): temperatures are either not sufficiently high before fracture, but are in the expected temperature range at fracture, or values for ΔT are sufficiently high before fracture, but then are unrealistically high at fracture. Therefore, and in accordance with previous reports [17,20,21,23], we conclude that adiabatic heating is not the cause of a drop in stress, but that mechanical work causes (due to the frictional sliding [58]) a temperature burst sufficiently high to provoke local melting even before fracture.

4.3. Description of the deformation kinetics during inhomogeneous flow

We recently described the phenomenological similarities of serrated flow behaviour in metallic glasses [31,32] with that of crystalline alloys which show the so-called dynamic strain aging (DSA) effect [33], more commonly known as the Portevin–LeChâtelier phenomenon. In the alloys studied here, similar to the DSA effect, we observe a transition from negative to positive SRS with decreasing temperature, which accompanies a change from serrated to smooth yielding (Fig. 8 and Table 1). Our results show that shear bands in metallic glasses exhibit a memory of their strain history, which is reflected by an increase in $\Delta\sigma$ with strain (see inset of Figs. 1, 7 or Table 2) and a decrease in the SRS at room temperature [30]. In DSA-deforming crystalline alloys such behaviour has been explained by considering the stress relaxation in the vicinity of a shear band [59].

In this section, we further describe details of the microscopic mechanism, which we believe is taking place during inhomogeneous deformation in BMGs. Recalling the dilatation models [7,24,25], large stress fields are suggested as causing a viscosity decrease (consequently promoting a stress drop), illustrating the strain dependency of the stress drop magnitude as well as the disappearance of serrations at lower temperatures (see Refs. [30,31] for a more detailed explanation). These models [7,24,25] do not, however, give satisfactory answers to the observed negative SRS and the decrease in the SRS with increasing strain [30,31]. Alternatively the model proposed here, which builds up on the above-mentioned models, allows for a interpretation of the experimental results. Fig. 10 illustrates schematically the concept of the model. Serrated flow can be understood as an alternating process of stress- and, as shown above, temperature-assisted shearing of atomic volumes (STZs) and a diffusive type of structural relaxation of these sheared volumes. With reference to the free volume model, the first process described is understood as a mechanism where free volume is generated (work softening), while in the second process free volume is annihilated (time-dependent hardening). Serrated flow can be correlated with shear offsets of several hundred nanometers (Fig. 9), while the shear of a single STZ is assumed to be of the order of Angstroms (see later results based on Eq. (7)). The process described below is believed to be a cooperative process where after the nucleation and initiation of STZs an avalanche effect is created, which adds up to submicrometer large shear offsets and macroscopically results in shear bands with a different structure than the bulk. As depicted in Fig. 10, after sufficient energy is provided for dilatation and generation of free volume a stress-assisted, thermally driven process in a shear transformation zone (① ② ③) and shear propagation (④) can take place. This process results in a stress release, plastic strain (shear band offset) and consequently the arrest of the distored structure (⑤). The second process triggers the annihilation of freshly free volume and therefore causes a *time-dependent* hardening of the area in the vicinity of the shear band. The waiting time t_{rel} between one and the next serration causes the alterated structure, or macroscopically speaking the shear band to recover and relax (⑥) to a lower energy state (i.e. higher density due to free volume annihilation) similarly as has been described in [58]. The rates of these counteracting processes lead to a positive net generation of free volume with increasing strain. Assuming a sudden decrease in the applied strain rate, more time is available for the relaxation to occur between successive stress drops. This time allows for the sheared zone to annihilate some of the freshly produced free volume. In turn this leads to a strengthening of the deformed zone or macroscopically speaking to a higher stress resistance against flow than attained by a more rapidly applied strain rate. Consequently, a higher flow stress results at lower applied strain rates producing a negative SRS. At liquid nitrogen temperatures, where m is positive and the flow curves are smooth, relaxation processes are hampered such that the rearranged atomic configuration cannot relax to a lower energy state after the shear event has taken place. We recently included this relaxation term (Δg) in the framework of the classical rate equation for thermally activated deformation processes in solids [31]. In this case, the shear strain rate is given by

$$\begin{aligned}\dot{\gamma} &= \dot{\gamma}_0 \exp\left(\frac{-\Delta G}{k_{\mathrm{B}} T}\right)\\ &= \dot{\gamma}_0 \exp\left(\frac{-(\Delta G_0 + \Delta g(T,\dot{\gamma},\gamma) - V_{\mathrm{ap}}\tau_{\mathrm{eff}})}{k_{\mathrm{B}} T}\right),\end{aligned} \qquad (6)$$

where $\dot{\gamma}_0$ is typically taken as the characteristic strain rate that depends on the frequency of sampling, and k_{B} and T are the Boltzmann constant and temperature, respectively. Note that due to the high applied stress, backward fluctuations are unlikely to occur. The Gibbs free energy required for the process to take place is equal to the difference between the total energy required (total energy barrier, ΔG_0), the energy state variable Δg and the work performed by the effective stress τ_{eff} on a volume V_{ap}. The latter, defined as the apparent activation volume, is

$$V_{\mathrm{ap}} = k_{\mathrm{B}} T \frac{\Delta \ln \dot{\gamma}}{\Delta \tau} \qquad (7)$$

and can be experimentally measured by strain rate jump or relaxation tests [59,60]. This quantity can be further related to the volume of a shear transformation zone (STZ) by $V_{\mathrm{ap}} = \Omega_0 \cdot \gamma_0$, where γ_0 is the critical strain of a STZ, which is of the order of 0.1 [7]. For Vit 105 ($Zr_{52.5}Ti_5Cu_{17.9}Ni_{14.6}Al_{10}$), V_{ap} increases with increasing strain rate from 0.15 to 0.23 nm^3 at 77 K, which yields STZs (Ω_0) of 70–120 atoms [61]. The values deduced here are of the same or-

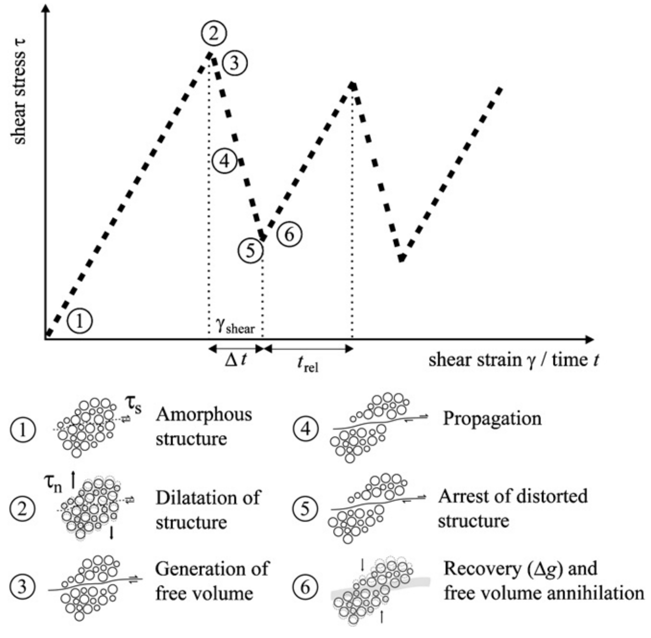

Fig. 10. Schematic illustration showing the proposed model for serrated flow in bulk metallic glasses (for more details see text).

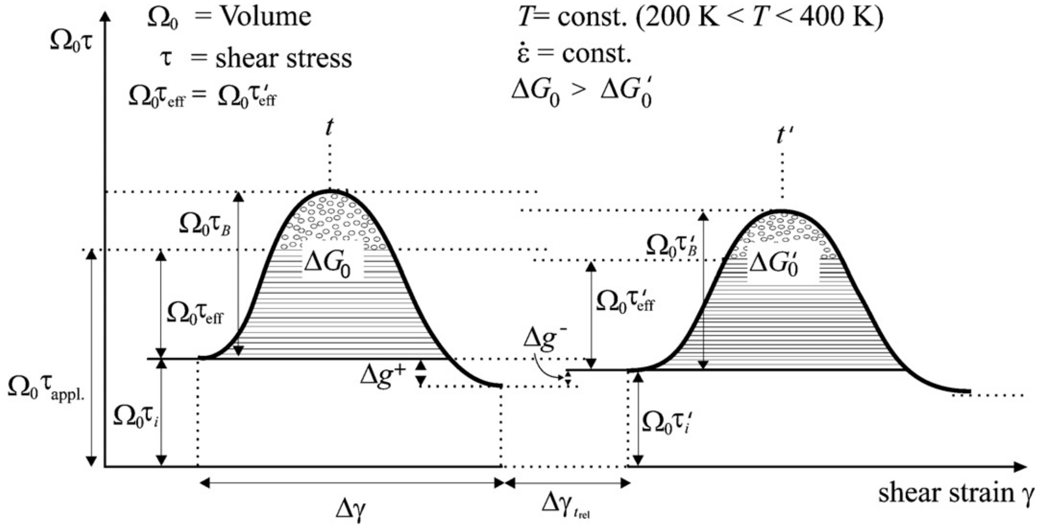

Fig. 11. Energy–strain diagram for the activation of two successive STZs at temperatures where serrated flow prevails. For simplicity, Ω_0 and the energy provided by the effective stress τ_{eff} is taken as a constant over strain. Δg^+ and Δg^- represent the energy resulting from the change in the atomic shear band structure by dilatation and by structural relaxation, respectively.

der of magnitude and are in very good accordance with recent theoretical models and molecular dynamic simulations, where the volume of a STZ has been identified to be in the range of 100–140 atoms [62–64]. The variable Δg, which depends on temperature, strain and strain rate, introduces the temporal evolution of the atomic structure (dilatation and structural relaxation) within shear bands after a shear event has taken place (i.e. in the absence of an effective stress). Fig. 11 shows the energy–strain diagram for the case of two successive shear events, where the regime of serrated flow prevails. It depicts the thermal energy barrier ΔG_0 ($\Omega_0\tau_B$) which must be overcome with the help of a temperature-/strain rate-dependent stress part, $\Omega_0\tau_{eff}$, and the assistance of thermal agitation (hatched and dotted areas in Fig. 11, respectively). Here, τ_i reflects the athermal stress contribution, which is equal to the internal stress. At 0 K all the energy would have to be provided by the applied stress in order to overcome ΔG_0, while at finite temperatures thermal agitation contributes to the process. After a shear event has taken place, the configuration of the atomic structure in the shear band changes towards a less dense structure, so that, irrespective of temperature, the energy barrier finds a new minimum energy (ground state) at ΔG_0–Δg^+. Nevertheless it should be noted that this more disordered configuration reflects a structure of elevated potential energy. At temperatures >200 K and after a sufficient amount of time (t_{rel}) prior to the next shear event, structural relaxation alters the configuration of atoms in the shear band enough that the ground state of the energy barrier changes by Δg^-, whereby $|\Delta g^+| > |\Delta g^-|$. Previous results[30] have shown that $m \propto 1/V_{ap}$ remains constant with strain at 77 K, but decreases only slightly at 300 K. For simplicity it is assumed here that the volume of a STZ remains constant with increasing strain. Therefore, in Fig. 11 the energy provided by the effective stress on the volume is assumed to be constant throughout the course of deformation, i.e. $\Omega_0\tau_{eff} \sim \Omega_0\tau'_{eff}$. However, the total energy ΔG_0 changes as a function of strain and temperature, so that $\Delta G_0 > \Delta G'_{0(300\ K)} > \Delta G'_{0(0\ K)}$. Consequently, both the appearance/disappearance of serrated flow and the observed negative SRS regime can be explained using Eq. (6). In addition, the proposed model explains well the disappearance of "pop-ins" at high indentation rates observed in nanoindentation experiments [1]. However, unlike the reasoning proposed in Ref. [1], we explain the absence of serrated flow by the inability of the shear band to relax (and thus to strengthen fast enough) rather than by a simultaneous activation of multiple shear bands.

5. Conclusions

Detailed high-resolution SEM and TEM observations of shear surfaces of deformed and unbroken BMG specimens exhibiting more than 20% strain were performed. The image information gained makes possible a detailed description of the shear surface morphology, and consequently a thorough interpretation of deformation kinetics and temperature influence during shear propagation before fracture. Apart from shear striations, few areas reveal typical vein pattern structures, but of more limited thickness (tens of nanometers) than those resulting at the moment of fracture (few micrometers). Calculations suggest that adiabatic heating alone does not explain these viscous structures, but that other non-adiabatic effects, such as friction and its release via stress drops causing an energy burst, are responsible for the temperature increase.

A microstructural kinetic model for thermally activated flow in BMGs has been presented, which explains the appearance and disappearance of serrated flow in conjunction with a change in the strain rate sensitivity from negative to positive values. Phenomenologically, such deformation behaviour has previously only been attributed to crystalline solids deforming via the Portevin–LeChâtelier effect. Within the framework of classical rate equations, a structural state variable (Δg) has been introduced, which accounts for the degree of structural relaxation occurring after a shear event has taken place and stresses are relieved. The variable Δg, which depends on temperature, strain and strain rate, reflects an energetic quantity for the appearance and disappearance of serrated flow that has not previously been considered in the literature of BMGs.

Acknowledgement

This work was supported by the Swiss National Science Foundation under Grant No. 200021-108071 (A.D.) and Grant No. 200021-105647 (F.H.D.T.).

References

[1] Schuh CA, Nieh TG. Acta Mater 2003;51:87.

[2] Schuster BE, Wei Q, Ervin MH, Hruszkewycz SO, Miller MK, Hufnagel TC, et al. Scripta Mater 2007;57:517.

[3] Pethica JB, Oliver WC. Mater Res Soc Proc 1989;130:13.

[4] Page TF, Oliver WC, McHargue CJ. J Mater Res 1992;7:450.

[5] Gerberich WW, Nelson JC, Lilleodden ET, Anderson P, Wyrobek JT. Acta mater 1996;44:3585.

[6] Corcoran SG, Colton RJ, Lilleodden ET, Gerberich WW. Phys Rev B 1997;55:16057.

[7] Argon AS. Acta Metall 1979;27:47.

[8] Volkert CA, Lilleodden ET. Phil Mag 2006;86:5567.

[9] Gouldstone A, Koh H-J, Zeng K-Y, Giannakopoulos E, Suresh S. Acta mater 2000;48:2277.

[10] Greer JR, Oliver WC, Nix WD. Acta Mater 2005;53:1821.

[11] Wright WJ, Saha R, Nix WD. Mater Trans JIM 2001;42:642.

[12] Kanungo BP, Glade SC, Asoka-Kumar P, Flores KM. Intermetall 2004;12:1073.

[13] Pampillo CA, Chen HS. Mat Sci Eng 1974;13:181.

[14] Masumoto T, Maddin M. Mater Sci Eng 1975;19:1.

[15] Bruck HA, Rosakis AJ, Johnson WL. J Mater Res 1996;11:503.

[16] Flores KM, Dauskardt RH. J Mater Res 1999;14:638.

[17] Hufnagel TH, Jaiao T, Li Y, Xing L-Q, Ramesh KT. J Mater Res 2002;17:1441.

[18] Yang B, Morrison ML, Liaw PK, Buchanan RA, Wang G, Liu CT, et al. Appl Phys Lett 2005;86:141904.

[19] Gilbert CJ, Ager III JW, Schroeder V, Ritchie RO, Lloyd JP, Graham JR. Appl Phys Lett 1999;74:3809.

[20] Wright WJ, Schwarz RB, Nix WD. Mater Sci Eng A 2001;319–321:229.

[21] Lewandowski JJ, Greer AL. Nat Mater 2006;5:15.

[22] Yang B, Liu CT, Nieh TG, Morrison ML, Liaw PK, Buchanan RA. J Mater Res 2006;21:915.

[23] Schuh CA, Hufnagel TH, Ramamurty U. Acta Mater 2007;55:4067.

[24] Cohen MH, Turnbull D. J Chem Phys 1959;31:1164. 1970;52:3038.

[25] Spaepen F. Acta Metall 1977;25:407.

[26] Gilman JJ. J Appl Phys 1973;44:675.

[27] Gilman JJ. J Appl Phys 1975;46:1625.

[28] Khonik VA, Spivak LV. Acta mater 1996;44:367.

[29] Khonik VA. Solid State Phenom 2003;89:67.

[30] Dalla Torre FH, Dubach A, Nelson A, Löffler JF. Mater Trans 2007;48:1774.

[31] Dubach A, Dalla Torre FH, Löffler JF. Phil Mag Lett 2007;87:695.

[32] Dalla Torre FH, Dubach A, Siegrist ME, Löffler JF. Appl Phys Lett 2006;89:091918.

[33] Mulford RA, Kocks UF. Acta Metall 1979;27:1125.

[34] Robinson JM, Shaw MP. Int Mater Rev 1994;39:113.

[35] Jin K, Löffler JF. Appl Phys Lett 2005;86:241909.

[36] Inoue A, Zhang W, Tsurui T, Yavari AR, Greer AL. Phil Mag Lett 2005;85:221.

[37] Das J, Tang MB, Kim KB, Theissmann R, Baier F, Wang WH, et al. Phys Rev Lett 2005;94:205501.

[38] Passchier CW, Trouw RA. Microtectonics. Berlin: Springer Verlag; 1996. p. 289.

[39] White SH, Burrows SE, Carreras J, Shaw ND, Humphreys FJ. J Struct Geol 1980;2:175.

[40] Siegrist ME, Amstad ED, Löffler JF. Intermet 2007;15:1228.

[41] Masumoto T, Maddin R. Acta Metall 1971;19:725.

[42] Donovan PE, Stobbs WM. Acta Metall 1981;29:1419.

[43] Pekarskaya E, Kim CP, Johnson WL. J Mater Res 2001;16:2513.

[44] Li J, Wang ZL, Hufnagel TC. Phys Rev B 2002;65:144201.

[45] Saida J, Setyawan ADH, Kato H, Inoue A. Appl Phys Lett 2005;87:151907.

[46] Kimura H, Masumoto T. Acta Metall 1983;31:231.

[47] Flores KM, Dauskart RH. J Mech Phys Sol 2006;54:2418.

[48] Glade SC, Busch R, Lee DS, Johnson WL, Wunderlich RK, Fecht HJ. J Appl Phys 2000;87:7242.

[49] Busch R, Kim YJ, Johnson WL, Rulison AJ, Rhim WK, Isheim D. Appl Phys Lett 1995;66:3111.

[50] Taylor GI, Quinney H. Proc Roy Soc Ser A 1934;143:307.

[51] Bai Y. Res Mech 1990;31:133.

[52] Eshelby JD, Pratt PL. Acta Metall 1956;4:560.

[53] Yamasaki M, Kagao S, Kawamura Y. Appl Phys Lett 2004;84:4654.

[54] Bengus VZ, Tabachnikova ED, Shumilin SE, Golovin YI, Makarov MV, Shibkov AA, et al. Int J Rapid Solid 1993;8:21.

[55] Vinogradov AYu, Khonik VA. Phil Mag 2004;84:2147.

[56] Löffler JF, Kündig AA, Dalla Torre FH. Rapid solidification and bulk metallic glasses—processing and properties. In: Groza JR, Shackelford JF, Lavernia EJ, Powers MT, editors. CRC materials processing handbook. Boca Raton, FL: CRC Press; 2007 [Chapter 17].

[57] Zhang Y, Greer AL. Appl Phys Lett 2006;89:071907.

[58] Shimizu F, Ogata S, Li J. Acta Mater 2006;54:4293.

[59] Dalla Torre FH, Pereloma EV, Davies CHJ. Acta Mater 2006;54:1135.

[60] Dalla Torre F, Spätig P, Schäublin R, Victoria M. Acta Mater 2005;53:2337.

[61] Dubach A, Dalla Torre FH, Löffler JF. Acta Mater [submitted for publication].

[62] Johnson WL, Samwer K. Phys Rev Lett 2005;95:195501.

[63] Zink M, Samwer K, Johnson WL, Mar SG. Phys Rev B 2006;73:172203.

[64] Mayr SG. Phys Rev Lett 2006;97:195501.